Soliton microcomb generation by cavity polygon modes

Botao Fu, Renhong Gao, Ni Yao, Haisu Zhang, Chuntao Li, Jintian Lin*,
Min Wang, Lingling Qiao, Ya Cheng*

Soliton microcomb generation by cavity polygon modes

Botao Fu, Renhong Gao, Ni Yao, Haisu Zhang, Chuntao Li, Jintian Lin, Min Wang, Lingling Qiao and Ya Cheng

---

Related articles

Flat soliton microcomb source
Xinyu Wang, Xuke Qiu, Mulong Liu, Feng Liu, Mengmeng Li, Linpei Xue, Bohan Chen, Mingran Zhang, Peng Xie
Opto-Electronic Science   2023 **2**, 230024   doi: 10.29026/oes.2023.230024

The real-time dynamic holographic display of LN:Bi,Mg crystals and defect-related electron mobility
Shuolin Wang, Yidong Shan, Dahuai Zheng, Shiguo Liu, Fang Bo, Hongde Liu, Yongfa Kong, Jingjun Xu
Opto-Electronic Advances   2022 **5**, 210135   doi: 10.29026/oea.2022.210135

Sub-femtometer-resolution absolute spectroscopy with sweeping electro-optic combs
Bingxin Xu, Xinyu Fan, Shuai Wang, Zuyuan He
Opto-Electronic Advances   2022 **5**, 210023   doi: 10.29026/oea.2022.210023

More related article in Opto-Electronic Journals Group website

Soliton microcomb generation by cavity polygon modes

Botao Fu[1,4], Renhong Gao[1,6], Ni Yao[2], Haisu Zhang[3], Chuntao Li[3], Jintian Lin[1,5]*, Min Wang[3], Lingling Qiao[1] and Ya Cheng[1,3,4,6,7]*

Soliton microcombs, which require the hosting cavity to operate in an anomalous dispersion regime, are essential to integrate photonic systems. In the past, soliton microcombs were generated on cavity whispering gallery modes (WGMs), and the anomalous dispersion requirement of the cavity made by normal dispersion material was achieved through structural dispersion engineering. This inevitably degrades the cavity optical quality factor (Q) and increases pump threshold power for soliton comb generation. To overcome the challenges, here, we report a soliton microcomb excited by cavity polygon modes. These modes display anomalous dispersion at near-infrared while optical Q factors exceeding 4×10^6 are maintained. Consequently, a soliton comb spanning from 1450 nm to 1620 nm with a record low pump power of 11 mW is demonstrated, a three-fold improvement compared to the state of the art on the same material platform.

Keywords: thin-film lithium niobate; nonlinear optics; microresonators

Introduction

Optical frequency comb (OFC) sees a plural of applications in building optical clocks, searching Earth-like exoplanets, exploring quantum optics, optical frequency synthesis, lidar, telecom communication, microwave photonics, and many others[1–9]. In recent years, on-chip soliton microcomb, which finely balances the dispersion with Kerr nonlinearity[1–3], has become one of the most important members of the comb family due to their high efficiency, compact size, robustness, and high repetition rate, providing new opportunities in miniaturizing and

has been demonstrated in various material platforms. To form a stable soliton pulse train in time for comb generation, the cavity is required to operate in an anomalous dispersion regime. In the past, such a requirement was fulfilled through structural dispersion engineering of the cavity whispering gallery mode (WGM), which is highly sensitive to geometrical dispersion and fabrication imperfection[10], leading to degraded Q-factors and higher pump threshold[11]. Moreover, in popular material platforms such as lithium niobate (LN)[12–16], which has high second-order nonlinearity and strong electro-optic effect[17–28], soliton comb generation can be easily impaired

¹State Key Laboratory of High Field Laser Physics and CAS Center for Excellence in Ultra-Intense Laser Science, Shanghai Institute of Optics and Fine Mechanics (SIOM), Chinese Academy of Sciences (CAS), Shanghai 201800, China; ²Research Center for Frontier Fundamental Studies, Zhejiang Lab, Hangzhou 311100, China; ³Engineering Research Center for Nanophotonics & Advanced Instrument, Ministry of Education, School of Physics and Electronic Science, East China Normal University, Shanghai 200241, China; ⁴School of Physical Science and Technology, ShanghaiTech University, Shanghai 200031, China; ⁵Center of Materials Science and Optoelectronics Engineering, University of Chinese Academy of Sciences, Beijing 100049, China; ⁶Shanghai Research Center for Quantum Sciences, Shanghai 201315, China; ⁷Hefei National Laboratory, Hefei 230088, China.

*Correspondence: JT Lin, E-mail: jintianlin@siom.ac.cn; Y Cheng, E-mail: ya.cheng@siom.ac.cn

Received: 18 May 2024; Accepted: 17 June 2024; Published online: 25 July 2024

by the competing stimulated Raman scattering due to its high Raman activities, causing even higher pump threshold power for soliton formation. For these reasons, the Kerr soliton microcomb has not yet been observed in single normal dispersion microresonators, allowing low pump power operation by leveraging the ultra-high Q factors.

Here, in contrast to using WGM, we generate soliton microcomb with a high-Q polygon mode. Excited by weak perturbations of a tapered fiber, cavity polygon modes are formed through the coherent combination of quasi-degenerate WGMs. Unlike the WGM counterpart, light in polygon modes propagates in a trajectory that is mostly away from the rough cavity edge and light coupling element. Consequently, the edge induced scattering loss is significantly reduced and the coupling loss is low even the tapered fiber is placed in contact with the cavity, leading to higher overall Q factor[29−32]. Meanwhile, the spatial distribution characteristics of polygon modes have small modal overlaps with other mode families, which further suppresses Raman effects and mode crossings. More importantly, compared with WGMs, polygon mode induced by weak perturbation is protected by the classical orbit, thus a lower dispersion occurs in polygon mode due to its stable geometrical conditions. As shown in this article, polygon modes possess anomalous group velocity dispersion (GVD) of −4.9 ps²/km even the fundamental WGM displays a normal dispersion of 25.5 ps²/km, enabling soliton microcomb ranging from 1450 nm to 1620 nm. Due to these advantages, an on-chip pump power threshold as low as 11.1 mW is recorded, which is only one third of the state of the art demonstrated on LN platform[25−28].

Soliton microcomb formation in high-Q LN microresonators by mode recombination

The fabrication of the normal dispersion LN microresonator

To demonstrate the Kerr soliton microcomb generation in the telecom band through coherent mode recombination, a Z-cut LN microdisk with transverse-electrically (TE) polarized fundamental WGMs under normal dispersion conditions is fabricated by photolithography assisted chemo-mechanical etching[12]. The details of the fabrication can be found in the Supplementary information Section S1. The microdisk possesses a radius of 62.3 μm, a wedge angle of 21°, a thickness of ~950 nm, and an ultra-smooth surface with roughness ~0.1 nm, as shown in the inset of Fig. 1(a).

Raman comb generated from fundamental WGM sequences with normal dispersion

We firstly pump the LN microdisk with the fundamental TE polarized WGM around 1561.32 nm via the tapered fiber with a diameter of 2 μm. The tapered fiber is placed in contact with the edge of the microdisk to couple the light into and out of the microdisk. The experimental setup can be found in the Supplementary information Section S2. Pump power is controlled at a low level to avoid nonlinear and thermo-optic effects for characterizing the mode structure. The transmission spectrum with the Lorentz profile in Fig. 1(a) shows a loaded Q factor Q_L of 3.0×10⁶ at 1561.32 nm. Figure 1(b) depicts the overall transmission spectrum of WGMs as a function of wavelength ranging from 1555 nm to 1570 nm, indicating a large number of high-order spatial WGM families exist within each free-spectral range (FSR) of the fundamental WGMs. Such dense high-order WGM families inevitably trigger mode crossing and stimulated Raman scattering when the fundamental WGM is pumped, due to the various Raman-active phonon bands in LN and high modal overlap between WGMs[12−16].

When the on-chip pump power is raised to 54.1 mW at 1561.33 nm, the Raman comb is observed with a broad spectral range, as demonstrated in Fig. 1(c). Several comb lines of high intensity within the broad envelope, corresponding to the Raman phonon frequency shifts of 235 cm⁻¹, 436 cm⁻¹, and 878 cm⁻¹ are observed. When the pump wavelength is blue detuned to the wavelength of 1561.31 nm, comb lines spanning over a broader spectrum range from 1450 nm to 2230 nm are generated due to the multiple and cascaded Raman scattering, as shown in Fig. 1(d). The FSR of the main comb lines around 1562 nm is 344.29 GHz, as depicted in Fig. 1(e). Moreover, several sub-comb lines between the adjacent main comb lines, which are resonant with spatial high-order WGMs induced by mode crossing, can be observed, as shown in Fig. 1(f). These spectra indicate the comb line phases are not mutually locked. In this condition, we are not able to generate the Kerr soliton because of the normal dispersion of fundamental WGMs as well as multiple strong Raman scattering and mode crossing.

Soliton comb generated from high-Q polygon mode sequences with anomalous dispersion by mode recombination

The difficulties in the generation of soliton microcomb can be overcome through the coherent combination of
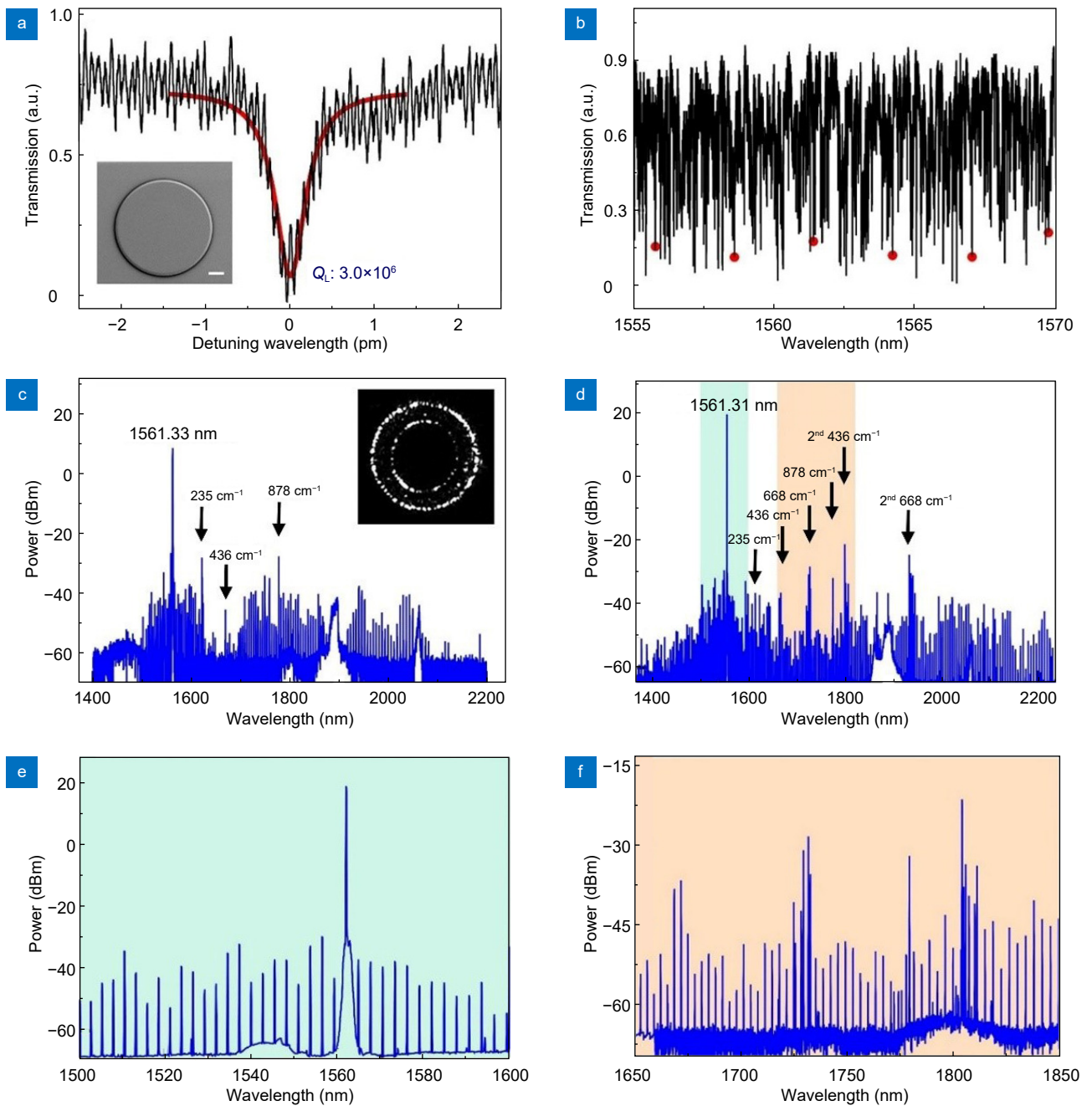
Fig. 1 | Raman comb generation. (**a**) The loaded *Q* factor of the fundamental WGM around 1561.32 nm wavelength. Inset: the scanning electron microscope (SEM) image of the fabricated microdisk, and the scale bar is 20 μm. (**b**) The transmission spectrum of the WGMs, where the fundamental mode family is labeled with red dots. (**c**) The spectrum of Raman comb when pumped at 1561.33 nm. Inset: The optical micrograph of the fundamental WGMs. (**d**) The spectrum of Raman comb when pumped at 1561.31 nm. (**e**) and (**f**) The enlarged spectral region labelled with the colored boxes in Fig. 1(d).

WGMs to satisfy anomalous dispersion conditions required by soliton comb formation in the LN microdisk. Here, we introduce such a mode control technique that can induce the formation of polygon mode protected by classical orbits through weak perturbations[29–32], thereby overcoming the influence of boundary curvature of the microdisk and significantly increasing the freedom in

setting soliton parameters. The details of the polygon mode formation utilizing the coherent mode recombination can be found in the Supplementary information Section S3. The polygon mode at the wavelength of 1542.80 nm is characterized by tunning the input wavelength across the resonance of the microdisk, and the measured loaded *Q* factor Q_L is 4.13×10⁶ by Lorentz fitting of the

transmission spectrum as shown in Fig. 2(a). This loaded Q factor is higher than that of the fundamental WGM because the polygon mode suffers from less scattering loss on its propagation path[29,32], which leads to a significant reduction of the pump power for soliton microcomb generation. The optical micrograph of the resonant mode confirms the formation of a square mode, as depicted in the inset of Fig. 2(a). It is worth noting that the polygon mode is frequently confined inside the microdisk and endures reduced defect from the microdisk sidewall, in comparison to the fundamental WGM. The mode spectrum obtained under the coupling condition of polygon mode is characterized by scanning the pump laser wavelength, as shown in Fig. 2(b). Although there are also lots of high-order modes within one FSR, once the pump light wavelength is tuned to excite one square mode, only the modes of sufficient spatial overlap with the square mode can be efficiently excited[29] through cascaded four-wave mixing processes for the soliton comb generation. The rest of the high-order modes, although

can in principle survive in the microdisk resonator, will have little chance of being excited with the pump laser due to the insufficient mode overlap between the two.

By scanning the input wavelength across the resonance from the red-detuned side to the blue-detuned side, the single-soliton comb spanning a spectral range from 1450 nm to 1620 nm is generated at the pump wavelength of 1542.79 nm and the on-chip pump power of 11.1 mW, which is confirmed by a smooth $sech^2$ shaped spectrum envelope, as presented in Fig. 2(c). The FSR of the comb lines is 374.31 GHz. Figure 2(d) shows the low-frequency radio-frequency (RF) noise spectrum of the soliton comb in Fig. 2(c). The $sech^2$ shaped envelope in Fig. 2(c) shows a flat spectrum extending to the direct-current (DC) end in Fig. 2(d), evidencing the coherent nature of the soliton state.

Numerical modeling

To understand the underlying physics behind the soliton comb generation in the polygon modes, the dispersion
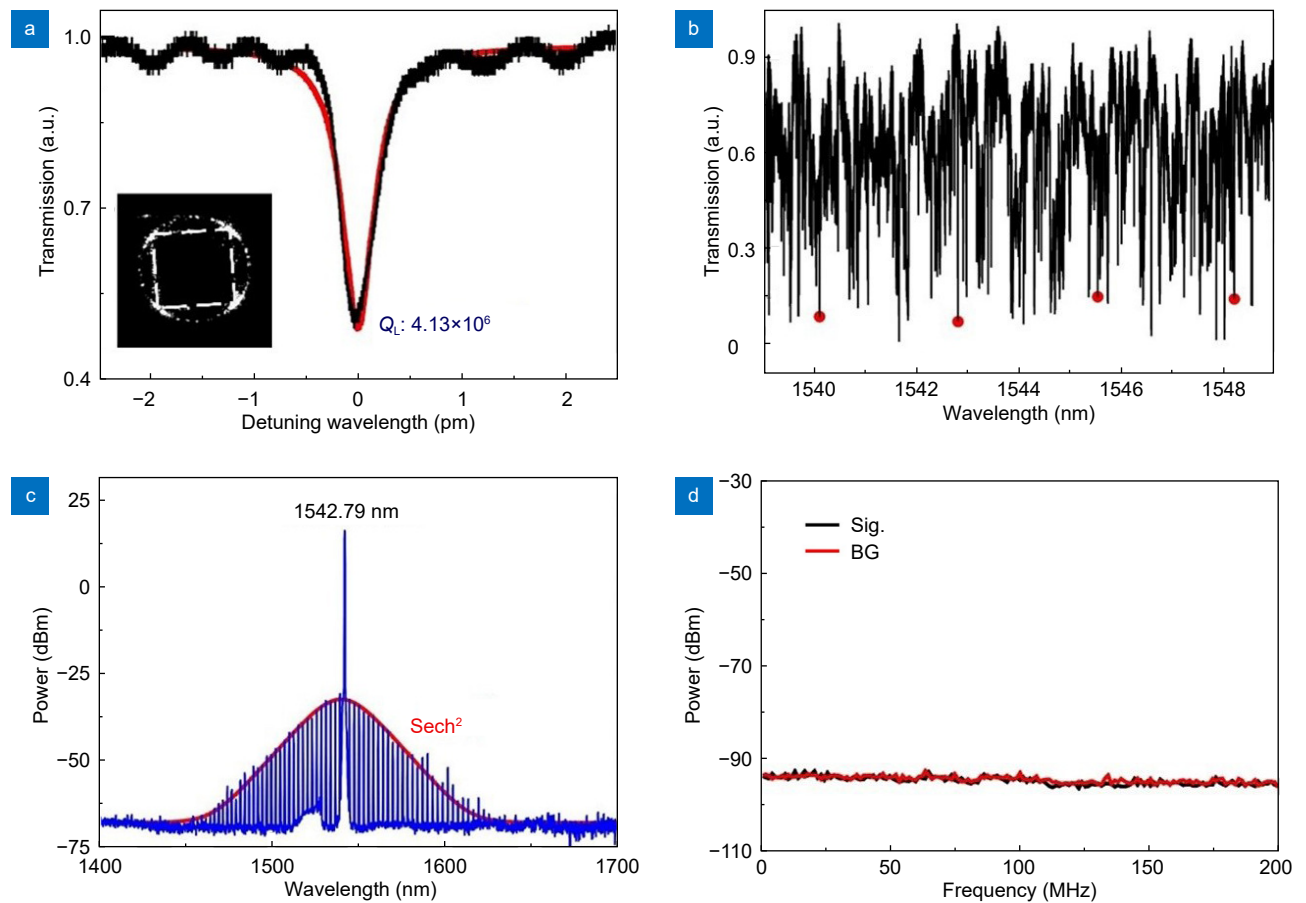

Fig. 2 | Soliton comb generation from polygon modes. (**a**) The measured loaded-Q factor of the mode around 1542.80 nm. Inset: the optical micrograph of the polygon modes. (**b**) The transmission spectrum of the square mode family (labelled with red dots). (**c**) The spectrum of the comb lines when pumping at 1542.79 nm. (**d**) The RF spectrum of soliton comb, where signal and background are denoted as Sig. and BG.
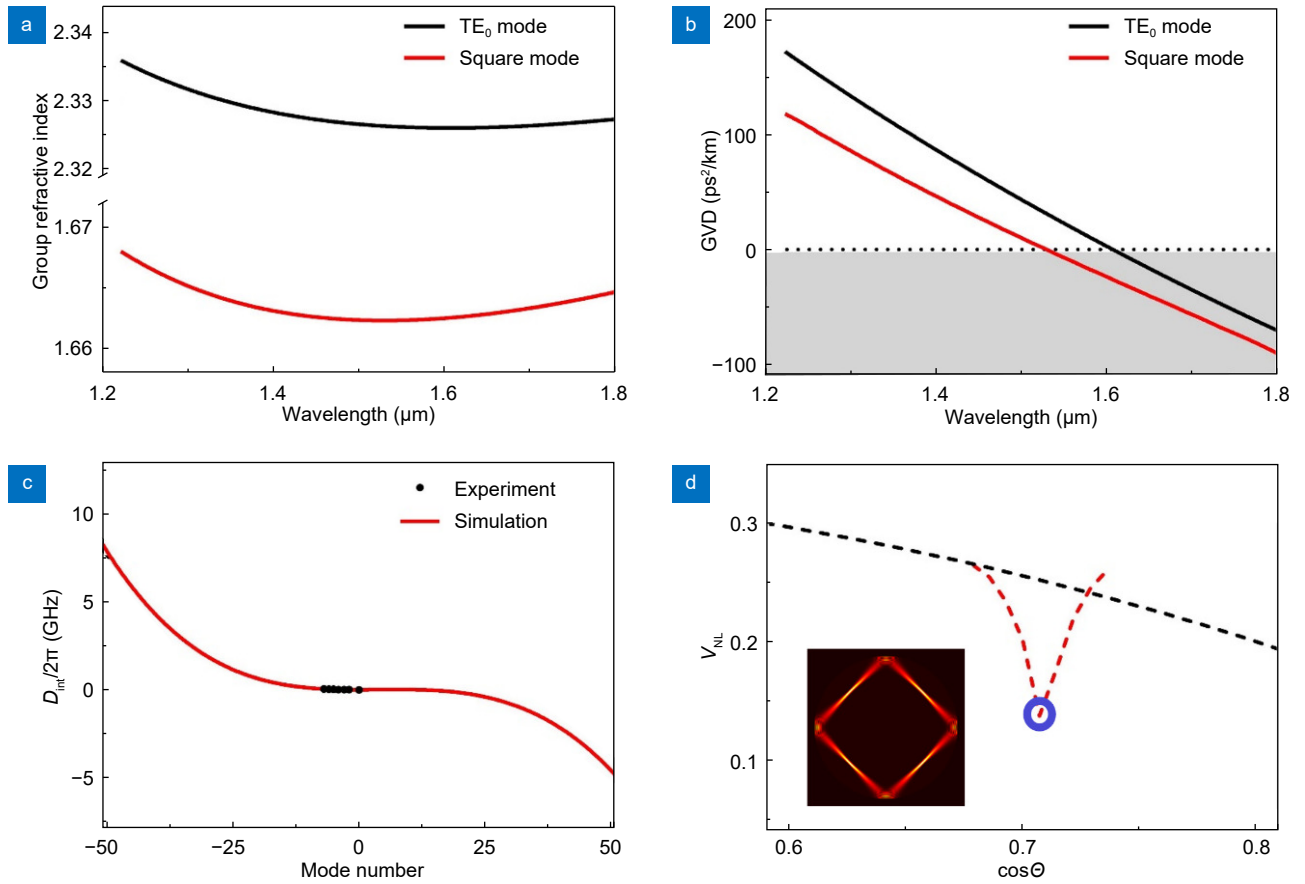
Fig. 3 | Dispersion design. (**a**) Simulated group refractive index curves. Here, the fundamental WGM TE$_0$ is denoted as TE$_0$ mode. (**b**) Simulated group velocity dispersion curves. (**c**) Simulated and its corresponding experimental integrated dispersion curves of the square modes, corresponding to the second-order dispersion $D_2/(2\pi)$ of 0.8 MHz. (**d**) The effective cavity nonlinear volumes of WGMs and square mode as a function of $\cos\Theta_{\lambda,R}$. Inset: the calculated mode profile of the polygon mode.

is calculated[31]. The effective index of the WGM can be expressed as follows,

$$n_{\text{eff}} = n\cos\Theta , \qquad (1)$$

where n and $\cos\Theta$ are the effective index of the thin film and the mode chord angle cosine, respectively. The $\cos\Theta$ can be represented by m/x, here m and $x = nkR$ are the azimuthal mode number and eigenvalue, and k and R are the wave vector in vacuum and the radius of the microdisk, respectively. $\cos\Theta$ represents the ratio of the angular momentum of the microdisk to the total momentum, which can be used to describe the modal geometrical characteristic. It is worth noting that the geometrical condition of the WGMs varies with the azimuthal mode number, and the modal dispersion of the WGM cannot be ignored in microdisks. In contrast, the formation of such polygonal modes relies on the equilibrium between quasi-degeneracy of WGMs within the microresonator and mode recombination induced by perturbation. Generally, the perturbation introduced by the optical ta-

pered fiber is exceedingly weak, primarily causing the exchange of components between adjacent eigenmodes with geometrical features closest to each other. The perturbation intensity solely hinges on the difference in relative quantum numbers, thereby resulting in the recombined modes possessing symmetry akin to classical orbits. The detailed comparison of the modal dispersion between the fundamental WGM and the square mode families can be found in the Section *Discussion*. The effective refractive index of the square mode can be expressed as,

$$n_{\text{eff}}^{\text{square}} = n_{\text{eff}} \frac{\cos\Theta_{\text{square}}}{\cos\Theta_{\lambda,R}} . \qquad (2)$$

Based on Eq. (1) and Eq. (2), the group refractive indices of fundamental TE$_0$ and square modes as functions of wavelengths are presented in Fig. 3(a). Simulated group velocity dispersion (GVD) curves of fundamental TE$_0$ and square modes are shown in Fig. 3(b). Here, the grey and blank regions indicate the anomalous dispersion

(GVD<0) and normal dispersion (GVD>0), respectively. The black dashed line represents the zero-dispersion point. We find that the fundamental mode TE_0 at 1550 nm wavelength is of a GVD of 25.5 ps^2/km, indicating the normal dispersion condition and in turn, hindering the comb generation. In contrast, the GVD of the square mode at 1550 nm is calculated to be −4.9 ps^2/km, featuring an anomalous dispersion. The striking difference indicates the feasibility of dispersion engineering utilizing the generation of the polygon mode. Figure 3(c) illustrates the integrated dispersion D_{int} of the TE_0 mode and square mode changes with relative mode number, which agrees well with the measured result denoted by black dots. Furthermore, the effective cavity nonlinear volumes[2] V_{NL} of the WGMs and square mode as a function of $cos\Theta_{\lambda,R}$ are compared in Fig. 3(d). Here the black and red dashed lines are WGMs and square modes with different excited states[31], respectively, and the blue circle represents the fundamental square mode. We find that the mode volume of the fundamental square mode is reduced significantly compared to the corresponding WGM, which reduces the threshold of comb generation.

Discussion

Generally, abundant quasi-degenerate modes exist in microresonator, the neighboring WGMs with the fixed angular quantum number difference with *N* allow the mode recombination, forming the polygon modes with *N*-fold symmetry. More details are discussed in ref.[31]. Generally, the weak perturbation introduced by the tapered fiber is not strong enough to cause longitudinal mode energy exchange, only involves the quasi-degenerated mode sequence recombination. To clearly describe the difference between WGMs and polygon modes, the mode distribution characteristics are demonstrated in Fig. 4. We observe that, the mode orbit is related to the mode eigenvalue, as plotted by Fig. 4(a). The mode distribution characteristics and close-up images of the WGM orbits for the relative mode numbers of −50, 0, and 50 of the fundamental WGM are shown in Fig. 4(b) and 4(c), respectively. Interestingly, the mode distribution depends on the relative mode number, thus modal dispersion is generated. In contrast, the formation of square orbit depends on the microresonator mode degeneracy controlled by classical orbit, thus the polygon mode is
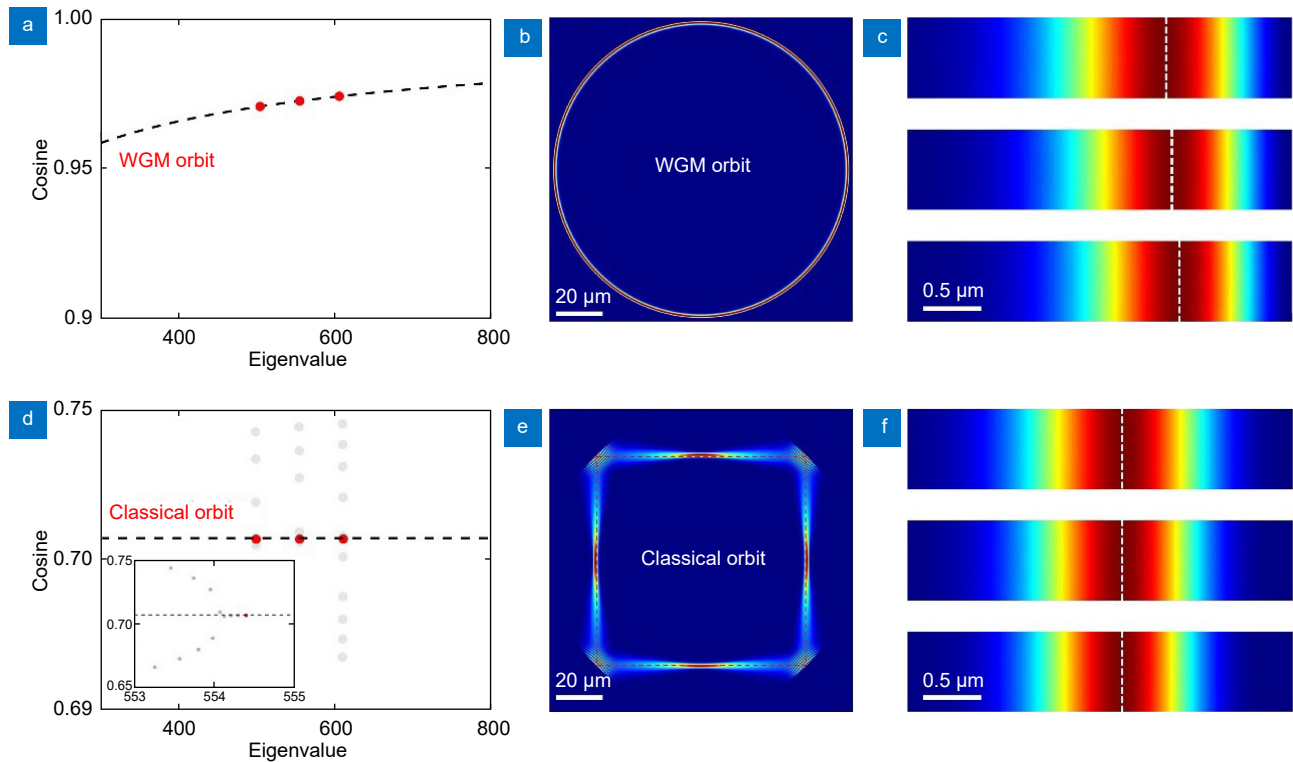

Fig. 4 | Comparison of geometrical features between the fundamental WGM and the square mode. (**a**) The WGM orbit cosΘ (Cosine) as a function of eigenvalue. (**b**) The mode distribution characteristics of fundamental WGM. (**c**) Close-up images of the WGM orbits for the relative mode numbers of −50, 0, and 50. (**d**) The classical orbit as a function of eigenvalue. (**e**) The mode distribution characteristics of the square mode. (**f**) Close-up images of the square orbits for the relative mode numbers of −50, 0, and 50.

constrained by the classical orbits under conditions when the perturbation depends only on the relative quantum number difference, as illustrated in Fig. 4(d). The mode distribution characteristics and close-up images of the square orbits for the relative mode numbers of −50, 0, and 50 are demonstrated in Fig. 4(e) and 4(f), respectively, validating the square mode is strictly limited by the classical orbits.

To further illustrate the evolution of the soliton comb generation, the laser wavelength is scanned from the red-detuned side of 1542.85 nm to the blue-detuned side of 1542.77 nm with a speed of 6.3 GHz/ms. When the laser pump wavelengths are set at 1542.83 nm and 1542.82 nm, four-wave mixing and cascaded four-wave mixing for spectral broadening are subsequently observed, as demonstrated in Fig. 5(a) and 5(b), respectively. When the laser wavelength is tuned to 1542.81 nm, the chaotic comb is generated as shown in Fig. 5(c), which is confirmed by the curvy low-frequency RF noise spectrum shown in the inset of Fig. 5(c). As the laser wavelength is further blue-detuned to 1542.79 nm wavelength, a soli-

ton step appears in the transmission spectrum as plotted in Fig. 5(d), in consistent with the soliton comb generation shown in Fig. 2.

To further improve the integration of the device, the tapered fiber can be replaced by an on-chip waveguide[33]. Generally, broadband anomalous dispersion engineering[34], ultra-high Q factors[35], spectral shaping and power amplification can be utilized to make the generated comb more practical.

Conclusions

In conclusion, we have demonstrated Kerr soliton generation in the LN microdisk of normal dispersion in the telecom band. Ultra-high Q polygon modes are coherently formed through coherent mode recombination and utilized to realize anomalous dispersion, which facilitate soliton comb generation with low pump power operation and greatly suppress the mode crossing and stimulated Raman scattering. Our technique makes the Kerr soliton microcomb generation insensitive to the geometrical dispersion of the microresonators, and allows higher
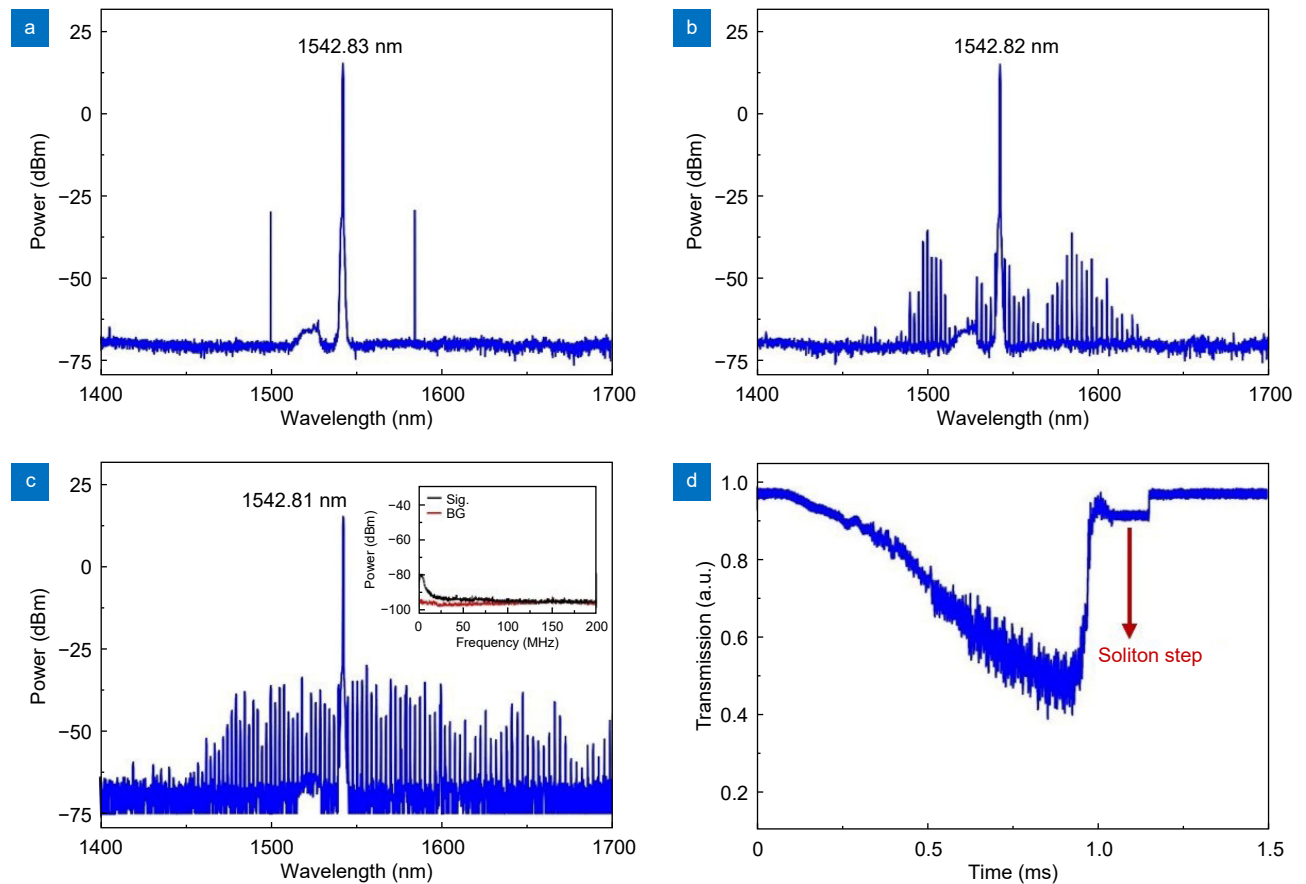

Fig. 5 | Evolution of the Kerr comb generation. (**a-c**) The spectra of the comb lines when tuning the pump wavelength from 1542.83 nm to 1542.81 nm. Inset in Fig. 5(c): the RF spectrum of chaotic comb. (**d**) The transmission spectrum during wavelength scanning, exhibiting a soliton step.

Q factors for low pump power operation, which has profound implication because otherwise there is an inevitable high price to pay for achieving a qualified microresonator that has an ultra-high Q factor and anomalous dispersion property, allowing soliton microcomb generated with low pump power.

References

1. Kippenberg TJ, Gaeta AL, Lipson M et al. Dissipative Kerr solitons in optical microresonators. *Science* **361**, eaan8083 (2018).
2. Herr T, Brasch V, Jost JD et al. Temporal solitons in optical microresonators. *Nat Photonics* **8**, 145–152 (2014).
3. Papp SB, Beha K, Del'Haye P et al. Microresonator frequency comb optical clock. *Optica* **1**, 10–14 (2014).
4. Liu JQ, Lucas E, Raja AS et al. Photonic microwave generation in the X- and K-band using integrated soliton microcombs. *Nat Photonics* **14**, 486–491 (2020).
5. Wang WQ, Wang LR, Zhang WF. Advances in soliton microcomb generation. *Adv Photonics* **2**, 034001 (2020).
6. Bai Y, Zhang MH, Shi Q et al. Brillouin-Kerr soliton frequency combs in an optical microresonator. *Phys Rev Lett* **126**, 063901 (2021).
7. Wan S, Niu R, Wang ZY et al. Frequency stabilization and tuning of breathing solitons in Si_3N_4 microresonators. *Photon Res* **8**, 1342–1349 (2020).
8. Chen HJ, Ji QX, Wang HM et al. Chaos-assisted two-octave-spanning microcombs. *Nat Commun* **11**, 2336 (2020).
9. Geng Y, Zhou H, Han XJ et al. Coherent optical communications using coherence-cloned Kerr soliton microcombs. *Nat Commun* **13**, 1070 (2022).
10. Moille G, Westly D, Orji NG et al. Tailoring broadband Kerr soliton microcombs via post-fabrication tuning of the geometric dispersion. *Appl Phys Lett* **119**, 121103 (2021).
11. Yuan ZQ, Gao MD, Yu Y et al. Soliton pulse pairs at multiple colours in normal dispersion microresonators. *Nat Photonics* **17**, 977–983 (2023).
12. Wu RB, Zhang JH, Yao N et al. Lithium niobate micro-disk resonators of quality factors above 10^7. *Opt Lett* **43**, 4116–4119 (2018).
13. Yu MJ, Okawachi Y, Cheng R et al. Raman lasing and soliton mode-locking in lithium niobate microresonators. *Light Sci Appl* **9**, 9 (2020).
14. Zhao YJ, Liu XY, Yvind K et al. Widely-tunable, multi-band Raman laser based on dispersion-managed thin-film lithium niobate microring resonators. *Commun Phys* **6**, 350 (2023).
15. Zhao GH, Lin JT, Fu BT et al. Integrated multi-color Raman Microlasers with ultra-low pump levels in single high-Q lithium niobate microdisks. *Laser Photonics Rev* **2024**, 2301328 (2024).
16. Gong Z, Li M, Liu XW et al. Photonic dissipation control for Kerr soliton generation in strongly Raman-active media. *Phys Rev Lett* **125**, 183901 (2020).
17. Jia YC, Wang L, Chen F. Ion-cut lithium niobate on insulator technology: Recent advances and perspectives. *Appl Phys Rev* **8**, 011307 (2021).
18. Lin JT, Bo F, Cheng Y et al. Advances in on-chip photonic devices based on lithium niobate on insulator. *Photon Res* **8**, 1910–1936 (2020).
19. Zhu D, Shao LB, Yu MJ et al. Integrated photonics on thin-film lithium niobate. *Adv Opt Photon* **13**, 242–352 (2021).
20. Huang YW, Feng J, Li YH et al. High-performance hyperentanglement generation and manipulation based on lithium niobate waveguides. *Phys Rev Appl* **17**, 054002 (2022).
21. Xue GT, Niu YF, Liu XY et al. Ultrabright multiplexed energy-time-entangled photon generation from lithium niobate on insulator chip. *Phys Rev Appl* **15**, 064059 (2021).
22. Xu MY, He MB, Zhang HG et al. High-performance coherent optical modulators based on thin-film lithium niobate platform. *Nat Commun* **11**, 3911 (2020).
23. Wang C, Zhang M, Yu MJ et al. Monolithic lithium niobate photonic circuits for Kerr frequency comb generation and modulation. *Nat Commun* **10**, 978 (2019).
24. Lu JJ, Puzyrev DN, Pankratov VV et al. Two-colour dissipative solitons and breathers in microresonator second-harmonic generation. *Nat Commun* **14**, 2798 (2023).
25. He Y, Yang QF, Ling JW et al. Self-starting bi-chromatic LiNbO3 soliton microcomb. *Optica* **6**, 1138–1144 (2019).
26. Wan S, Wang PY, Ma R et al. Photorefraction-assisted self-emergence of dissipative Kerr solitons. *Laser Photonic Rev* **18**, 2300627 (2024).
27. Gong Z, Liu XW, Xu YT et al. Soliton microcomb generation at 2 μm in z-cut lithium niobate microring resonators. *Opt Lett* **44**, 3182–3185 (2019).
28. Yang C, Yang S, Du F et al. 1550-nm band soliton microcombs in Ytterbium-doped lithium-niobate microrings. *Laser Photonics Rev* **17**, 2200510 (2023).
29. Lin JT, Farajollahi S, Fang ZW et al. Electro-optic tuning of a single-frequency ultranarrow linewidth microdisk laser. *Adv Photonics* **4**, 036001 (2022).
30. Gao RH, Fu BT, Yao N et al. Electro-optically tunable low phase-noise microwave synthesizer in an active lithium niobate microdisk. *Laser Photonics Rev* **17**, 2200903 (2023).
31. Fu BT, Gao RH, Lin JT et al. Modes trimming and clustering in a weakly perturbed high-Q whispering gallery microresonator. *Laser Photonics Rev* **17**, 2300116 (2023).
32. Farajollahi S, Fang ZW, Lin JT et al. Multimode perturbation modeling for cavity polygon and star modes. *Phys Rev A* **108**, 033520 (2023).
33. Guan JL, Li CT, Gao RH et al. Monolithically integrated narrow-bandwidth disk laser on thin-film lithium niobate. *Opt Laser Technol* **168**, 109908 (2024).
34. Li Q, Briles TC, Westly DA et al. Stably accessing octave-spanning microresonator frequency combs in the soliton regime. *Optica* **4**, 193–203 (2017).
35. Gao RH, Yao N, Guan JL et al. Lithium niobate microring with ultra-high Q factor above 10^8. *Chin Opt Lett* **20**, 011902 (2022).

Acknowledgements

Author contributions

J. T. Lin and Y. Cheng conceived the experiments, B. T. Fu and N. Yao performed the simulation, R. H. Gao and C. T. Li fabricated the LN microdisks, N. Yao produced the tapered fiber, R. H. Gao, B. T. Fu and J. T. Lin carried out the experiment and measurement, B. T. Fu, J. T. Lin, M. Wang, H. S. Zhang, and L. L. Qiao analyzed the data. N. Yao, H. S. Zhang, J. T. Lin, and Y. Cheng wrote the manuscript with input from all co-authors. Y. Cheng, M. Wang, and J. T. Lin supervised the project. All authors contributed extensively to the work presented in this paper.

Competing interests

The authors declare no competing financial interests.

Supplementary information

Supplementary information for this paper is available at
https://doi.org/10.29026/oea.2024.240061

Scan for Article PDF